Shear Resistance of an Auxetic Chiral Mechanical Metamaterial

Shengguang Jin[1], Yannis P. Korkolis[2], and Yaning Li[1]*

[1] Department of Mechanical Engineering, University of New Hampshire, Durham NH 03824, USA

[2] Department of Integrated Systems Engineering, The Ohio State University, Columbus OH 43210, USA

Abstract

The shear resistance of 3D printed periodic auxetic chiral mechanical metamaterial was quantified via a picture-frame apparatus. The experimental set-up allowed the accurate measurement of the effective shear modulus of the material. Also, a rigid-rod-rotational spring model shows that the effective shear modulus of the material is directly related to the chiral geometry and the rotational rigidity of the center joints and the corner joints in the chiral cell. To facilitate practical design, design guidelines were developed through an integrated analytical, numerical and experimental approach. The influences of the chiral geometry and the joint rigidity on the shear resistance of the periodic auxetic chiral mechanical metamaterial were quantified. The design guidelines were verified by systematic finite element (FE) simulations.

Keywords: shear; auxetic chiral mechanical metamaterial; picture frame; 3D printing;

1. Introduction

The shear modulus, also called modulus of rigidity, is an important material property to describe the resistance of materials to the change of shape under shearing load. While the bulk modulus is to quantify the material resistance to the volume change under pressure. It is known that for homogenous isotropic materials, the Poisson's ratio is related to the material rigidity corresponding to shape change and volume change. For example, for rubbery materials with Poisson's ratio close to 0.5, it is easy to change the shape while hard to change the volume; thus, these materials have high bulk modulus and low shear modulus. As an opposite version of rubbery materials, materials with negative Poisson's ratio (auxetic materials) can easily change the volume but are hard to change the shape; therefore, low bulk modulus and high shear modulus is expected for auxetic materials (Evans and Alderson, 2000; Carneiro et al., 2013; Novak et al., 2016;).

*yaning.li@unh.edu

As a fast-developing new category of materials, different types of artificial auxetic mechanical metamaterials have emerged, including auxetic open cell solids (Lakes, 1987; Friis et al., 1988; Yeganeh-Haeri et al., 1992), two-phase composites (Evans et al., 1992; Alderson et al., 2005; Li et al., 2018). Among all of them, auxetic cellular solids are one important category due to their light weight, excellent indentation resistance , energy absorption capability, and unique acoustic and optical properties (Scarpa et al., 2003; Tee et al., 2010; Bückmann et al., 2012). Recently, numerous innovative designs of auxetic mechanical metamaterials have appeared, with a focus on exploring new mechanisms for auxeticity. For example, instability-induced auxetic effects were identified for both 2D and 3D porous material (Bertoldi et al., 2010; Babaee et al., 2013) ; chirality-induced auxetic effects were quantified via mechanical experiments on 3D printed specimens (Jiang and Li, 2017); more recently, by utilizing the chirality-induced rotation, auxetic chiral mechanical metamaterials with a new sequential cell-opening mechanism were developed and proved via 3D printing (Jiang and Li, 2018a; Jiang and Li, 2018b).

In previous studies, the effective mechanical properties of auxetic foams were characterized via analytical, numerical and experimental approaches. Some of them focus on the Poisson's ratio and/or effective stiffness under uniaxial loading only (Chung and Wass, 1999; Bertoldi et al., 2010; Babaee et al., 2013; Hou et al., 2014; Li et al., 2018). Some of them also explored the shear resistance. For example, the transverse shear modulus of in-plane re-entrant honeycombs is determined via numerical simulations (Scarpa and Tomlin, 2000); the out-of-plane linear elastic mechanical properties of trichiral, tetrachiral and hexachiral honeycombs were explored via analytical, finite element simulations and experiments on samples produced with FDM and SLS rapid prototyping machines (Lorato et al., 2010); the mechanical properties including Young's and shear moduli and the Poisson's ratio of both conventional and re-entrant copper foams were examined by resonant ultrasound spectroscopy (RUS) (Li et al., 2013); and recently, the shear modulus of open cell polyurethane thermoformed auxetic foams was identified from three- and four-point bending tests on sandwich beams with the foams as the cores (Cheng et al., 2019).

Through a discrete asymptotic homogenization method, Reis and Ganghoffer (2012) derived closed form solutions for the effective properties of auxetic lattices. However, in that paper, the auxetic lattices were modeled as structures composed of Bernoulli beams. Therefore, when the ribs of the lattices have low slenderness, the bending effects can not be predicted accurately. Also, it is expected that the mechanical behavior of the physical joints between neighboring ribs in the

real lattices can not be accurately quantified through the joints between Bernoulli beams. To facilitate practical design, more sophisticated analytical and numerical models are needed.

In this investigation, an integrated experimental, numerical and analytical modeling approach was developed to evaluate the mechanical behaviors of auxetic cellular solids under shear. To facilitate practical design of the material, sophisticated analytical and numerical models were developed. In the analytical model, the joints between two neighboring ribs were modeled as rotational springs. In this way, the mechanical behavior of the joints in the real material can be predicted more accurately. In the finite element model, two dimensional plane stress elements were used; therefore, compared with the beam element model, the bending effects of the ribs can be captured well. Also, to generate an overall pure shear deformation under small deformation, a picture-frame apparatus was designed and fabricated via 3D printing. A 3D printed auxetic chiral mechanical metamaterial was employed as an example material system for the methodology developed.

In the literature, the auxetic chiral mechanical metamaterial explored in this paper was called missing rib structure (Smith et al., 2000; Gaspar et al., 2005; Jiang and Li, 2017) or cross chiral structure (Reis and Ganghoffer, 2012, Magalhaes et al., 2016; Lu et al., 2017). It is known that for this type of design, the auxetic effect is due to the rotation of the cell (Smith et al., 2000; Reis and Ganghoffer, 2012; Jiang and Li, 2017). Recently, through a hybrid design strategy of adding soft corners and/or stiffer cores to the original missing rib/cross chiral design, the internal rotation efficiency of the cells can be elevated and therefore the auxetic effects can be amplified (Jiang and Li, 2017; Jiang and Li, 2018a; Jiang and Li, 2018b). Based on the micropolar elasticity, a closed-form solution for the effective properties of missing-rib/cross-chiral structure was derived (Bahaloo and Li, 2019).

Tracing back to 1960s, picture-frame shear test was developed as a biaxial testing approach to determine the in-plane shear stiffness and strength of plywood panels (Bryan, 1960). Via a picture frame shear apparatus, a uniform pure shear stress state can be generated within the tested specimen at small deformation (Ogden, 1984). Thus, when loading the specimen in a picture frame apparatus, the intrinsic shear modulus of the material can be measured from the load-displacement relation (Mohammed et al., 2000; Zhang et al., 2000; Cao et al., 2004; Liu et al., 2005; Cao et al., 2008). Due to easy implementation and great accuracy, the picture frame test has been widely used

in the mechanical characterization of the in-plane shear resistance of textile materials such as woven fabrics (Cao et al., 2004; Cao et al., 2008; Liu et al., 2005; Mohammed et al., 2000; Zhang et al., 2013), fiber reinforced composites (Wittenberg et al., 2001; Nostrat-Nezami et al., 2004), and foam-like materials (Diel et al., 2014), under both small and large deformations. For example, Cao et al. (2008), characterized the material property of woven fabric composite through picture frame shear test through a collaborative effort . Chen et al. (2011), used the picture frame test to explore the in-plane shear behavior of fiber reinforced composites (Carbon/Polyphenylene Sulfide) at different processing temperatures . Diel et al. designed and fabricated a shear fixture to determine both shear strength and stiffness of a cellular foam (2014). Their testing results validated the accuracy of the fixture and proved the pure shear stress state within the specimen loaded with the fixture under small deformation (Diel et al., 2014).

However, so far, little efforts were made on conducting shear tests on auxetic cellular solids via the picture-frame test. Due to the auxetic effect, potential detaching between specimen and the apparatus is expected. The picture-frame test needs to be appropriately adjusted to accommodate this unique mechanical behavior of the auxetic material. In this investigation, the shearing resistance of 3D printed chiral auxetic cellular solids will be measured via a customized 3D printed picture frame apparatus for auxetic materials.

2. Mechanical experiments

2.1. The design and fabrication of a chiral specimen

A periodic chiral auxetic cellular solid with four-fold symmetry was designed, as shown in Fig. 1a. The dimensions of the representative volume element (RVE) of the periodic solid are also shown in Fig.1a. The specimen consists of 5x5 RVEs. In order to connect the specimen to a picture frame apparatus (details are provided in Section 3), thin frames with buttons were added at the boundaries of the specimen. The specimen was then fabricated under room temperature via a multi-material 3D printer (Objet Connex 260). To minimize the printing time, the specimen was printed layer by layer through the depth direction. Model material DM9760 (a digital material with Young's modulus ~2.75MPa) was used for the major part of the specimen, and TangoBlack (a soft rubbery material with Young's modulus ~0.78MPa) was used for the thin edge frames and buttons. The specimen was cured in room temperature for 48 hours before mechanical experiments.

2.2. Picture-frame experiments

A picture frame apparatus was designed via the computer aided engineering (CAE) software SolidWorks and then it was fabricated in a 3D printer (Dimension SST 1200es). The apparatus was printed as ABS+ material (a hard-plastic material, with Young's modulus ~2.5GPa). The apparatus is shown in Fig. 2. The major parts of the apparatus are four loading plates connected via lubricated pins at the corners. The top and bottom connecters were also designed to link the picture frame apparatus to a Zwick/Roell material testing machine (zwickiLine).

During the experiments, the bottom connector was fixed on the testing machine and the top connector was moved up to load the specimen. To rule out the influence of friction and the weight of the apparatus, the force-displacement relation of the picture frame apparatus only (without the specimen) was subtracted from the curve with the specimen. A 100N load cell was used. Then, quasi-static experiments were performed by controlling the vertical displacement rate of the top connecter to be $\sim 0.015 mm/s$. The overall shear strain was calculated from the uni-axial displacement measured (Eq. A4 in the Appendix A). A high-resolution camera was used to record the deformed configuration of the specimen (1image/2500ms). The effective shear modulus can be calculated from the load-displacement curve (details are provided in **Appendix A**).

3. Finite element simulations

Different from the beam element model of the cross chiral structure developed by Reis and Ganghoffer (2012), a two-dimensional FE model with multiple parts was developed in ABAQUS/CAE. As shown in Fig. 3, the three parts include the major portion of the specimen (grey), the thin frame and buttons (red), and the four loading plates of the apparatus (green). The thin frame and buttons were perfectly bonded with the major portion of the specimen, while hard contact with a friction coefficient of 0.01 was defined between the boundaries of thin frame and buttons and the loading frames. Two-dimensional four node plane stress elements (CPS4) were used in all parts. To determine the mesh size, a mesh refinement study was performed.

In all FE simulations, two types of boundary conditions were used and compared: (1) to simulate the experiment, the neighboring pieces of loading frames were kinematically-coupled at points *T*, *B, L* and *R*, as shown in Fig.3b. A prescribed vertical displacement δ was applied at point *T*, while the bottom *B* was constrained vertically. To avoid rigid body movement of the specimen in the horizontal direction, the horizontal displacement of the center node of the chiral specimen was constrained. In the parametric study, periodic boundary conditions (PBC) were used to get the

intrinsic material properties of the chiral cellular solid. The FE results from the two types of boundary conditions were compared.

FE simulations were conducted in the implicit finite element software ABAQUS/STANDARD v6.13. The hyperelastic Mooney-Rivlin model was used to simulate materials DM9760 and TangoBlack. The strain energy density function of the Mooney-Rivlin model is:

$$W = C_{10}(I_1 - 3) + C_{01}(I_2 - 3)\,, \tag{1}$$

where I_1 and I_2 are the first and second invariants of stretch tensor. For DM9760, $C_{10} = 0$ MPa and $C_{01} = 0.46$ MPa and for TangoBlack, $C_{10} = 0.031$ MPa and $C_{01} = 0.099$ MPa. Thus, the shear modulus of DM9760 is 0.92 MPa and that of TangoBlack is 0.26 MPa.

4. Analytical model

4.1. A rigid-rod-rotational-spring model

The representative volume element (RVE) of the chiral cellular solid can be modeled as a system of rigid rods and rotational springs. The geometry of the RVE is shown in Fig. 4a. The overall dimensions of the RVE are L_1 and L_2. The chiral cell in the RVE is composed of six rigid ribs, including two long ribs, *HD* and *BF* (Fig. 4a), in the middle with length 2*l*, forming a cross at center *O*, and four short ribs with length *l*, *AB*, *CD*, *EF* and *GH*, connecting to the middle two. The long ribs and the neighboring short ribs form an angle α_o in the initial configuration. The two long ribs are connected at *O* via a center rotational spring with stiffness K_φ. The four short ribs are connected to the long ribs through four corner rotational springs with stiffness K_α, as shown schematically in Fig. 4b.

4.2 Pure shear deformation

Pure shear is an irrotational strain with body elongation in one direction and shortening orthogonally. Simple shear is an isochoric plane deformation in which parallel planes translate relative to each other with a constant distance. Both require no area changes, but pure shear involves no rigid body rotation, while simple shear does. In real world, most of the shear deformation is a combination of both. For picture frame tests, under small deformation, it is very close to pure shear.

As shown in Fig. 4a, shearing traction is applied at the top, bottom, left and right boundaries of the RVE. During the deformation, the angles at *B* and *F* will change by $d\alpha$, and the angles at *H* and *D* will change by $d\beta$. The center spring with stiffness K_φ will deform by $d\varphi$.

Thus, the virtual strain energy of the rigid-rod-rotational-spring system can be expressed as

$$\delta U = 2\left(\frac{1}{2}K_\alpha d\alpha^2\right) + 2\left(\frac{1}{2}K_\alpha d\beta^2\right) + \frac{1}{2}K_\varphi(2d\varphi)^2 = \frac{1}{2}\bar{G}\gamma^2 L_1 L_2\,, \tag{2}$$

where $\alpha = \alpha_0 + d\alpha$, $\beta = \alpha_0 + d\beta$ and γ and $\bar{G}$ are the shear strain and effective shear modulus of the RVE, respectively.

At small deformation, it is assumed that, $d\alpha = -d\beta$, and the magnitudes of both $d\alpha$ and $d\beta$ are smaller than $d\varphi$. Thus, Eq. (2) becomes

$$\delta U = 2K_\alpha d\alpha^2 + 2K_\varphi d\varphi^2\,. \tag{3}$$

The virtual work of the system is

$$\delta W = 2P_1\delta u + 2P_2\delta u\,, \tag{4}$$

where P_1 and P_2 are the applied forces at *A*, *E*, *G* and *C*, and as shown in Fig. 4a, δu is the virtual horizontal displacement at points *A, E*, and virtual vertical displacements at *G* and *C*. Through kinematics, δu is related to the overall shear strain γ as

$$\delta u \cong \sin\left(\frac{\gamma}{2}\right)\left(2l\sin\frac{\alpha_0}{2}\right) \tag{5}$$

The principle of virtual work requires $\delta U = \delta W$. According to Eqs. (2)-(5) and the detailed derivation in **Appendix A**, the effective shear modulus $\bar{G}$ can be derived as:

$$\bar{G} = \frac{K_\alpha\left(\frac{d\alpha}{d\varphi}\right)^2 + K_\varphi}{\left(\frac{\gamma}{d\varphi}\right)^2\left(8l^2\sin^2\frac{\alpha_0}{2}\right)}\,. \tag{6}$$

Force equilibrium and kinematics (detailed derivations are provided in **Appendix B**) of the ribs yield:

$$R_K = \frac{K_\varphi}{K_\alpha}, \frac{d\alpha}{d\varphi} = \frac{R_K}{4}, \text{and } \frac{\gamma}{2} = d\varphi, \tag{7}$$

where R_K is defined as the stiffness ratio between the center spring and the corner spring. The effective shear modulus can be normalized by the center spring stiffness K_φ as:

$$\frac{\bar{G}}{K_\varphi} = \frac{\frac{R_K}{16} + 1}{32l^2 sin^2\left(\frac{\alpha_o}{2}\right)}. \tag{8}$$

Through the rigid-rod-rotational spring model, the effective stiffness $\bar{E}$ was derived as:

$$\frac{\bar{E}}{K_\varphi} = \frac{(\frac{1}{R_K} + \frac{1}{R_K + 8})}{2l^2 cos^2\left(\frac{\alpha_o}{2}\right)}. \tag{9}$$

Thus, the ratio between the effective shear modulus and the effective stiffness is derived as a function of the stiffness ratio R_K of the center and corner springs and the corner angle α_o:

$$\frac{\bar{G}}{\bar{E}} = \frac{\frac{R_K}{8} + 2}{\left(\frac{1}{R_K} + \frac{1}{R_K + 8}\right)[32tan^2\left(\frac{\alpha_o}{2}\right)]}. \tag{10}$$

According to Eq. (10), the ratio $\overline{G}/\overline{E}$ between the effective shear modulus and the effective stiffness is plotted in Fig. 5. It can be seen that generally, when the spring stiffness ratio R_K increases, $\overline{G}/\overline{E}$ increases, and when the corner angle α_o decreases, $\overline{G}/\overline{E}$ increases. The results indicate that when R_K increases, and/or α_o decreases, the chiral cell becomes more resistant to shear than to uni-axial loading.

5. Results and discussion

5.1. Experimental and FE results

Experimental snapshots of the deformed specimen at overall shear strains of 5° (0.087 rad.), 10° (0.18 rad.) and 15° (0.26 rad.) are shown in Fig. 6. The corresponding FE contours of the maximum principal strain for two different types of boundary conditions are shown in Fig. 6b and 6c, respectively. It can be seen that the FE results from the two types of boundary conditions are

consistent. Also, when the overall shear strain increases, the deformation becomes more and more concentrated in the center joint.

The curves of shear stress vs. shear strain from the experiments and FE simulations are compared in Fig. 7. It can be seen that at small overall shear strain $\gamma \leq 3^{\circ}$ $(0.052\ rad.)$ the curves are almost identical. This confirms the fact that under small deformation, the picture frame apparatus creates a stress state very close to pure shear for this periodic cellular solid. When strain increases, the FE curve with the experimental boundary conditions becomes slightly higher than the experimental one. While the FE curve with periodic boundary conditions becomes slightly lower than the experimental one. These differences are due to the boundary effects and the generation of micro damages in the specimen during deformation. Also, in experiments, under deformation beyond $\gamma \approx 15^{\circ}$ $(0.26\ rad.)$ due to the auxetic effect, the buttons and channels start to separate. This indicates that the designed buttons are necessary to hold the specimen and the loading frames together during the deformation.

To further evaluate the influences of the added thin frame and buttons around the specimen on experimental measurements, the strain energy associated within each part in the FE model is shown in Fig. 8. It can be seen that during the deformation, about 90% of the strain energy developed in the major part of the specimen, the loading plates barely absorb energy, and the thin frame and buttons absorb about 10% of the total strain energy.

The effective shear modulus obtained from the experiments and FE simulations are compared in **Table 1**. The FE and experimental results are consistent.

5.2 Geometry effects

Based on Eq. (10), the effective shear modulus to effective Young's modulus ratio is determined by the spring stiffness ratio K_{φ} and the corner angle α_o. To facilitate practical design, the relationship between the model parameter R_K and the design parameters of the RVE needs to be explored. Thus, by varying the rib thickness t, the rib length l, the corner angle α_o, a systematic set of FE simulations were performed. For FE models, two-dimensional, plane stress elements were used. Incompressible hyperelastic Mooney-Rivlin model was used for the digital material (DM9760) from the 3D printer. Both the effective shear modulus and the Young's modulus for chiral cells with different geometries can be obtained from these FE simulations. When the

geometric parameters of a RVE are $l = 5mm, t = 0.2mm$ *and* $\alpha_o = 90^\circ$, from the model, the spring stiffness ratio of this RVE is determined as $R_{K_o} = 3.6$. By taking the RVE with R_{K_o} as a reference, the influences of the rib thickness *t*, the rib length *l*, and the corner angle α_o on the model parameter R_K can be evaluated via the relative difference between R_K and R_{K_o} , as shown in Figs. 9a, 9b and 9c, respectively.

Figure 9a shows that when *l* and α_o are fixed ($l = 5$ mm and $\alpha_o = 90^\circ$) and the rib thickness *t* increases from 0.1mm to 3mm, the stiffness ratio R_K slightly increases (<4.69%). Figure 9b shows that when *t* and α_o are fixed ($t = 0.2$ mm and $\alpha_o = 90^\circ$) and the rib length *l* increases from 1mm to 10mm, R_K slightly decreases. And the difference ranges from -1.70% to 2.25%. Similarly, Figure 9c demonstrates that the stiffness ratio R_K increases slightly when α_o increases from 60° to 120° and *t* and *l* are fixed ($t = 0.2$ mm and $l = 5$ mm). The difference is within 4.80% range. Therefore, in the design space explored, the model spring stiffness ratio R_K is barely influenced by the rib thickness *t*, the rib length *l* and the corner angle α_o.

5.3 Soft hinge effects

Although the stiffness ratio R_K is not sensitive to geometry of the chiral cell, in practical design, it can be tuned in a large range by adding soft materials at the corners or a harder core in the center (Jiang and Li, 2017). It is known that for chiral auxetic cells, by adding the soft hinges at the corners and/or harder core at the center, both the auxeticity and the effective stiffness of the chiral cell can be tailored in a very wide range (Jiang and Li, 2017). This soft hinge effect on the shear resistance of the auxetic chiral cell can be quantified via the current model and systematic FE simulations. To evaluate this effect, two-dimensional FE models with soft corners were developed. The geometry of the model is $l = 5$ mm, $t = 0.2$ mm, $\alpha_o = 90^\circ$. The rib material was modeled by the hyperelastic Mooney-Rivlin model (model parameters are the same as those for DM9760) and the stiffness ratio between the rib material and material at the corner was varied from 1 to 1000, both the effective shear modulus and effective stiffness were obtained from the FE simulations under small deformation ($\gamma < 0.0018\, rad.\, [0.1^\circ]$ and $\varepsilon < 0.001$). According to Eq. (10) and the FE results, the stiffness ratio R_K of the rotational springs is positively related to the stiffness ratio E_r/E_h between the rib material and the material at the soft corners, as shown in Fig. 10a.

According to Fig. 10a, empirically, R_K can be related to E_r/E_h via a power law

$$R_K = C_1\left(\frac{E_r}{E_h} - 1\right)^m + C_2\,, \tag{11}$$

where $C_1 = 0.237, m = 0.703$. It can be seen that when $\frac{E_r}{E_h} = 1$, $R_K = C_2 = 3.6$.

Equations (10) and (11) provide a design guideline to tailor the $\bar{G}/\bar{E}$ ratio of the auxetic chiral cellular solid. To further support this guideline, FE models with five different corner angles ($\alpha = 60^\circ, 75^\circ, 90^\circ, 105^\circ$ and 120°) and different stiffness ratios E_r/E_h were developed. The model prediction (Eqs. (10) and (11)), shown as solid lines, and the FE results, shown as solid circles, are compared in Fig. 10b. It can be seen that in a large design space, the model results match with the FE results very well.

6. Conclusions

In this investigation, the shear resistance of 3D printed periodic auxetic chiral mechanical metamaterial was quantified via a customized picture-frame apparatus. To avoid potential detachment between the auxetic specimen and the apparatus, it was found necessary to design soft interlockings at the boundaries of the specimen. Finite element simulations with periodic boundary conditions verified that the new experimental set up can accurately measure the intrinsic shear modulus of the material.

Also, a rigid-rod-rotational spring model was used to derive an analytical solution to predict the influences of the chiral geometry and the rotational rigidity of the center and corner joints on the shear resistance of the chiral cell. It was found that the ratio between the effective shear modulus and the effective stiffness of the auxetic chiral mechanical metamaterial is determined by the corner angle α_o and the stiffness ratio R_K of the center and corner springs. Generally, when R_K increases, and/or α_0 decreases, the ratio between the effective shear modulus and the effective stiffness of the auxetic chiral mechanical metamaterial can be increased significantly.

In addition, to facilitate practical design, systematic FE simulations were performed to explore the relationships between the physical design parameters and the key model parameters R_K. It was found that the model parameter R_K is barely influenced by the geometric parameters of the chiral cell, including the rib thickness, rib length, and the corner angle α_o. However, R_K is very sensitive to the stiffness ratio between the rib material and the material at the corner joints. Based on the

FE results and model prediction, an empirical power law relation was identified to quantify the relation between the model parameter R_K and the stiffness ratio between the rib material and the material at the corner joints.

Acknowledgement

Y.L. and S.J. acknowledge the supports from NSF through grants CMMI-1554468 (CAREER), DoD/AFOSR through grant FA9550-16-1-0011, and NSF through grant EPSCoR-1757371 (NH Bio-Made). S.J. also acknowledges the Summer Undergraduate Research Fellowship (SURF) fellowship at the University of New Hampshire (UNH). We also acknowledge the contribution of Mohammad Jahedi who worked at UNH under the financial support from UNH Center for Advanced Materials and Manufacturing Innovation (CAMMI).

Appendix A. Measuring effective shear modulus via the picture-frame apparatus

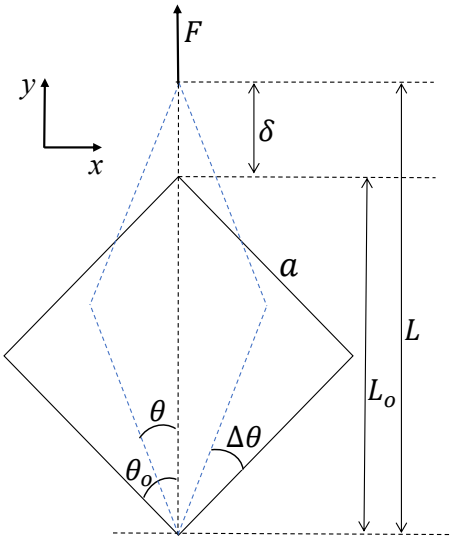

Fig. A1: The schematic drawing of the picture frame apparatus (black square represents the undeformed configuration and blue diamond is the deformed configuration).

The schematic drawing of the picture-frame shear is shown in Fig. A1. The initial configuration of the picture frame with edge length a is shown in Fig. A1 as a square. The four edges of the picture frame are linked via friction-free pins at the four corners. The diagonal line of the square is along the vertical direction in the global coordinate x-y. Due to the tensile load at the top corner, the picture-frame will deform from a square with initial angle $\theta_0 = 45^{\circ}$ into a diamond with angles 2θ and $\pi - 2\theta$ in the current configuration, as shown in Fig. A1. Thus, the shearing strain is equal to the change in angle. L_0 ($L_0 = \sqrt{a}$) and L ($L = 2acos\theta$) are the vertical diagonal length of the apparatus in the undeformed and deformed configurations, respectively. In experiments, the bottom corner is fixed, and δ and F are the vertical displacement and uniaxial force applied at the top corner of the apparatus, respectively. Thus, the shear stress on the specimen can be determined from the applied force F and the geometry of the apparatus in the deformed configuration as:

$$\tau = \frac{F}{(2at)cos\theta}, \tag{A1}$$

where t is the out-of-plane depth of the apparatus. The measured displacement δ is related to the current angle θ as:

$$\delta = L - L_0 = a(2cos\theta - \sqrt{2})\,. \tag{A2}$$

Hence,

$$\theta = arccos\left(\frac{\delta}{2a} + \frac{\sqrt{2}}{2}\right). \tag{A3}$$

The overall shear strain is related to θ as:

$$\gamma = 2(\theta_0 - \theta) = 90^{\circ} - 2arccos\left(\frac{\delta}{2a} + \frac{\sqrt{2}}{2}\right). \tag{A4}$$

According to Eqs. A2 and A4, the effective shear modulus $\bar{G}$ of the specimen can be obtained from the measured F and δ as:

$$\bar{G} = \frac{\tau}{\gamma} = \frac{F}{2atcos\theta\left[90^{\circ} - 2arccos\left(\frac{\delta}{2a} + \frac{\sqrt{2}}{2}\right)\right]}. \tag{A5}$$

Appendix B. Derive the effective shear modulus of a chiral cell via a rigid-rod-rotational-spring model

To derive Eq. (6), due to four-fold symmetry of the chiral cell,

$$P_1 = P_2 = P\,. \tag{B1}$$

Also,

$$L_1 = L_2 = L = 4lsin\left(\frac{\alpha_o}{2}\right). \tag{B2}$$

The effective shear modulus $\bar{G}$ is calculated as the ratio between the shear stress and shear strain

$$\bar{G} = \frac{\tau}{\gamma}\,. \tag{B3}$$

The effective shear stress τ of the RVE can be calculated as

$$\tau = \frac{P}{L}\,. \tag{B4}$$

B1. Kinematics

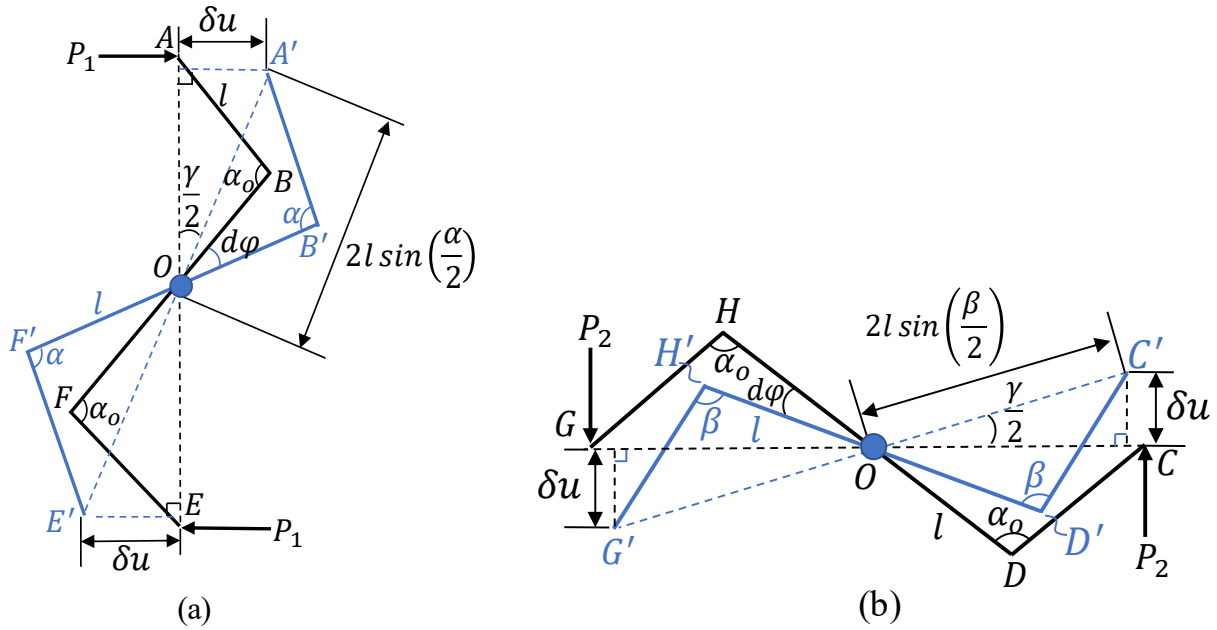

Fig. B1: Kinematics of the: (a) vertical ribs; (b) horizontal ribs. Initial configuration (black), and after shearing deformation (blue).

From the geometry shown in Fig. B1a, at small deformation

$$\delta u = \sin\left(\frac{\gamma}{2}\right)\left(2lsin\frac{\alpha}{2}\right) \cong \sin\left(\frac{\gamma}{2}\right)\left(2lsin\frac{\alpha_o}{2}\right), \tag{B5}$$

Similarly, Fig. B2b shows that after infinitesimal shearing deformation,

$$\delta u = \sin\left(\frac{\gamma}{2}\right)\left(2lsin\frac{\beta}{2}\right) \cong \sin\left(\frac{\gamma}{2}\right)\left(2lsin\frac{\alpha_o}{2}\right), \tag{B6}$$

Thus,

$$2K_\alpha d\alpha^2 + 2K_\varphi d\varphi^2 = [4(\bar{G}\gamma L)][sin\left(\frac{\gamma}{2}\right)\left(2lsin\frac{\alpha_o}{2}\right)]. \tag{B7}$$

By rearranging equation B7, the effective shear modulus $\bar{G}$ becomes

$$\bar{G} = \frac{K_\alpha d\alpha^2 + K_\varphi d\varphi^2}{16\gamma\, sin\left(\frac{\gamma}{2}\right)\left(lsin\frac{\alpha_o}{2}\right)^2}. \tag{B8}$$

The small angle approximation gives,

$$\lim_{\frac{\gamma}{2}\to 0} sin(\frac{\gamma}{2}) \approx \frac{\gamma}{2} . \qquad (B9)$$

Incorporating equation B9, equation B8 becomes,

$$\bar{G} = \frac{K_\alpha(\frac{d\alpha}{d\varphi})^2 + K_\varphi}{(\frac{\gamma}{d\varphi})^2(8l^2 sin^2\frac{\alpha_o}{2})} . \qquad (B10)$$

In equation 10, the only unknown parameters are $\frac{d\alpha}{d\varphi}$ and $\frac{\gamma}{d\varphi}$. Force equilibrium and kinematic relation of the ribs were invoked to solve for these unknowns.

B2. Force equilibrium

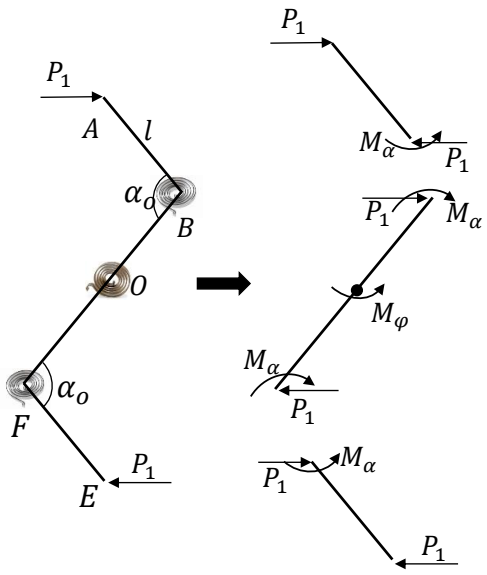

Fig. B2: Force equilibrium of the vertical ribs.

The free body diagram of the vertical ribs is shown in Fig. B2. The equilibrium of ribs *AB* and *FE* yields,

$$M_\alpha = K_\alpha(d\alpha) = P_1\left[l\,sin\left(\frac{\alpha_o}{2}\right)\right] . \qquad (B11)$$

The equilibrium of rib *BF* yields,

$$M_\varphi = K_\varphi d\varphi = 2M_\alpha + 2P_1\left[l\,sin\left(\frac{\alpha_o}{2}\right)\right] = 4K_\alpha(d\alpha) . \qquad (B12)$$

Hence

$$\frac{d\alpha}{d\varphi} = \frac{R_K}{4}. \tag{B13}$$

B3. Kinematic relation

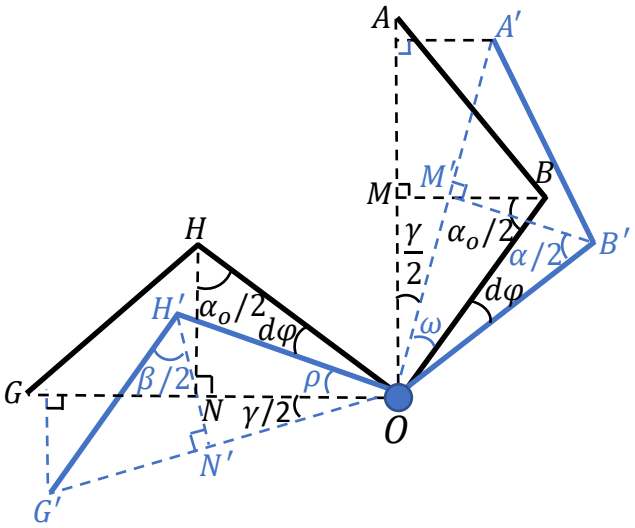

Fig. B3: Kinematic relations of: (a) vertical ribs *AB* and *BO*; (b) horizontal ribs *GH* and *HO*. Initial configuration (black) and after shearing deformation (blue).

As shown in Fig. B3 in triangle *BMO* of the initial configuration, it is shown that

$$\omega = 90^{\circ} - \frac{\gamma}{2} - \frac{\alpha_o}{2}. \tag{B14}$$

In the triangle $B'M'O$ of the deformed geometry,

$$\omega = 90^{\circ} - d\varphi - \frac{\alpha}{2}. \tag{B15}$$

After combining Eqs B14 and B15, it yields

$$\frac{\gamma}{2} = d\varphi + \frac{d\alpha}{2}. \tag{B16}$$

Based on the empirical simulation results, an important assumption is made here when comparing the magnitude between $d\alpha$ and $d\varphi$ as

$$\frac{d\alpha}{2} \ll d\varphi\,. \qquad (B17)$$

Then equation B17 becomes

$$\frac{\gamma}{2} = d\varphi. \qquad (B18)$$

Likewise, the same conclusion (equation B18) can be obtained for the triangle $H^{'}N^{'}O$ and HNO after combining equation B19 and B20.

$$\rho = 90^{\circ} - \frac{\gamma}{2} - \frac{\beta}{2}, \qquad (B19)$$

$$\rho = 90^{\circ} - d\varphi - \frac{\alpha_o}{2}. \qquad (B20)$$

References

Alderson, K.L., Simkins, V.R., Coenen, V.L., Davies, P.J., Alderson, A., Evans, K.E., 2005. How to make auxetic fibre reinforced composites. Physica Status Solidi (B) Basic Research, 242 (3), 509–518.

Babaee, S., Shim, J., Weaver, J.C., Chen, E.R., Patel, N., Bertoldi, K., 2013. 3D soft metamaterials with negative Poisson's ratio. Advanced Materials 25 (36), 5044–5049.

Bahaloo, H., Li, Y., 2019. Mircopolar modeling of auxetic chiral lattices with tunable internal rotation. Journal of Applied Mechanics 86 (4), 041002.

Bertoldi, K., Reis, P.M., Willshaw, S., Mullin, T., 2010. Negative Poisson's ratio behavior induced by an elastic instability. Advanced Materials 22 (3), 361–366.

Bryan E. 1960. Photoelastic evaluation of the panel shear test for plywood. ASTM STP289 (American Society for Testing and Materials) 1961:90-94.

Bückmann, T. et al. 2012. Tailored 3D Mechanical Metamaterials Made by Dip-in Direct-Laser-Writing Optical Lithography. Advanced Materials. 24 (20): 2710–2714.

Cao, J., Akkerman, R., Boisse, P., Chen, J., Cheng, H.S., de Graaf, E.F., Gorczyca, J.L., Others, 2008. Characterization of mechanical behavior of woven fabrics: Experimental methods

and benchmark results. Composites Part A: Applied Science and Manufacturing 39 (6), 1037–1053.

Cao, J., Cheng, H.S., Yu, T.X., Zhu, B., Tao, X.M., Lomov, S.V., Others, 2004. A cooperative benchmark effort on testing of woven composites. Proceedings of the 7th Int ESAFORM Conference on Material Forming, 305–308.

Carneiro, V.H., Meireles, J., Puga, H., 2013. Auxetic materials - A review. Materials Science-Poland 31 (4), 561–571.

Cheng, H.C., Scarpa, F., Panzera, T.H., Farrow, I., Peng, H., 2019. Shear Stiffness and Energy Absorption of Auxetic Open Cell Foams as Sandwich Cores. Macroscopic Auxetic Materials & Models, 256, 1800411, 1–9.

Chen, Q., Boisse, P., Park, C.H., Saouab, A., Bréard, J., 2011. Intra/inter-ply shear behaviors of continuous fiber reinforced thermoplastic composites in thermoforming processes. Composite Structures 93 (7), 1692–1703.

Chung, J., Waas, A.M., 1999. Compressive response and failure of circular cell polycarbonate honeycombs under inplane uniaxial stresses. J. Eng. Mater. Technol. 121 (4), 494-502.

Diel, S., Huber, O., Steinmann, P., Winter, W., 2014. Design and validation of a new fixture for the shear testing of cellular solids. Archive of Applied Mechanics 84 (3), 309–321.

Evans, K.E., Alderson, A., 2000. Auxetic materials: Functional materials and structures from lateral thinking! Advanced Materials 12 (9), 617–628.

Evans, K.E., Nkansah, M.A., Hutchinson, I.J., 1992. Modelling negative Poisson's ratio effects in network-embedded composites. Acta Metallurgica et Materialia 40 (9), 2463-2469.

Friis, E.A., Lakes, R.S., Park, J.B., 1988. Negative Poisson’s ratio polymeric and metallic foams. Journal of Material Science 23 (12), 4406–4414.

Gaspar, N., Ren, X.J., Smith, C.W., Grima, J.N., Evans, K.E., 2005. Novel honeycombs with auxetic behavior. Acta Mater., 53 (8), 2439–2445.

Hou, Y., Neville, R., Scarpa, F., Remillat, C., Gu, B., Ruzzene, M., 2014. Graded conventional-auxetic Kirigami sandwich structures: flatwise compression and edgewise loading. Composite Part B: Engineering 59, 33-42.

Jiang, Y., Li, Y., 2017. 3D printed chiral cellular solids with amplified auxetic effects due to elevated internal rotation. Advanced Engineering Materials 19 (2).

Jiang, Y., Li, Y., 2018a. Novel 3D-printed hybrid auxetic mechanical metamaterial with chirality-induced sequential cell opening mechanisms. Advanced Engineering Materials 20 (2).

Jiang, Y., Li, Y., 2018b. 3D printed auxetic mechanical metamaterial with chiral cells and reentrant cores. Scientific Reports 8 (1), 2397.

Lakes, R.S., 1987. Foam structures with a negative Poisson's ratio. Science 235 (4792), 1038–1040.

Li, D., Dong, L., Lakes, R.S., 2013. The properties of copper foams with negative Poisson's ratio via resonant ultrasound spectroscopy. Physica Status Solidi (b), 250 (10), 1983–1987.

Li, T., Chen, Y., Hu, X., Li, Y., Wang, L., 2018. Exploiting negative Poisson's ratio to design 3D-printed composites with enhanced mechanical properties. Materials & Design 142, 247–258.

Liu, L., Chen, J., Li, X., Sherwood, J., 2005. Two-dimensional macro-mechanics shear models of woven fabrics. Composites Part A: Applied Science and Manufacturing 36 (1), 105–114.

Lorato, A., Innocenti, P., Scarpa, F., Alderson, A., Alderson, K.L., Zied, K.M., Ravirala, N., Miller, W., Smith, C.W., Evans, K.E., 2010. The transverse elastic properties of chiral honeycombs. Composites Science and Technology, 70 (7), 1057–1063.

Lu, Z., Wang, Q., Li, X., Yang, Z., 2017. Elastic properties of two novel auxetic 3D cellular structures. International Journal of Solids and Structures, 124, 46–56.

Magalhaes, R., Subramani, P., Lisner, T., Rana, S., Ghiassi, B., Fangueiro, R., Lourenco, P.B., Oliveira, D.V., Lourenco, P.B., 2016. Development, characterization and analysis of auxetic structures from braided composites and study the influence of material and structural parameters. Composites: Part A, 87, 86–97.

Mohammed, U., Lekakou, C., Dong, L., Bader, M.G., 2000. Shear deformation and micromechanics of woven fabrics. Composites Part A: Applied Science and Manufacturing 31 (4), 299–308.

Nosrat-Nezami, F., Gereke, T., Eberdt, C., Cherif, C., 2014. Characterization of the shear-

coupling of carbon-fiber fabric under controlled membrane tensions for precise simulative predictions of industrial preforming processes. Composites Part A: Applied Science and Manufacturing 67, 131–139.

Novak, N., Vesenjak, M., Ren, Z., 2016. Auxetic cellular materials - a Review. Strojniški Vestnik – Journal of Mechanical Engineering 62 (9), 485–493.

Ogden, R.W., 1984. Non-linear elastic deformations. New York.

Reis, F. Dos, Ganghoffer, J.F., 2012. Equivalent mechanical properties of auxetic lattices from discrete homogenization. Computational Materials Science, 51 (1), 314–321.

Scarpa, F., Tomlin, P.J., 2000. On the transverse shear modulus of negative Poisson' s ratio honeycomb structures. Fatigue Fract. Engng. Mater. Struct., 23 (8), 717-720.

Scarpa, F., Dallocchio, F., Ruzzene, M., 2003. Identification of Acoustic Properties of Auxetic Foams. P. Soc. Photo-Opt. Ins. 5052, 468-474.

Smith, C.W., Grima, J.N., Evans, K.E., 2000. A novel mechanism for generating auxetic behavior in reticulated foams: missing rib foam model. Acta Mater., 48 (17), 4349-4356.

Tee, K.F., Spadoni, A., Scarpa, F., Ruzzene, M., 2010. Wave Propagation in Auxetic Tetrachiral Honeycombs. J. Vib. Acoust. 132(3).

Wittenberg, T.C., van Baten, T.J., de Boer, A., 2001. Design of fiber metal laminate shear panels for ultra-high capacity aircraft. Aircraft Design 4 (2–3), 99–113.

Yeganeh-Haeri, A., Weidner, D.J., Parise, J.B., 1992. Elasticity of α-cristobalite: a silicon dioxide with a negative Poisson's ratio. Science 257 (5070), 650-652.

Zhang, Y., Sun, F., Wang, Y., Chen, L., Pan, N., 2013. Study on intra/inter-ply shear deformation of three dimensional woven preforms for composite materials. Materials & Design 49, 151–159.

Figure Captions:

Fig. 1: Dimensions of the (a) specimen in a 2D view, (b) in a 3D view and (c) channels of the fixtures: $L = 50mm$.

Fig. 2: The picture-frame apparatus: (a) solid model; (b) the 3D printed assembly.

Fig. 3: The FE model: (a) assembly and the mesh, and (b) boundary conditions and the prescribed displacement.

Fig. 4: The schematic drawing of the model RVE under pure shear: (a) the undeformed configuration (black lines) and the deformed configuration (blue lines); (b) the rigid-rod-rotational spring model of an RVE.

Fig. 5: The ratio between the effective shear modulus and the effective stiffness vs. R_K for various corner angle α_o, predicted by Eq. (10).

Fig. 6: (a) Snapshots of the deformed specimen from the experiments at the overall shear strain of $\gamma \approx 5^{\circ}$, 10°, and 15°; and the corresponding FE contours of the maximum principal strain with the boundary conditions the same as the experiment (b), and those with periodic boundary conditions (c).

Fig. 7: Shear stress-shear strain curves. The lines refer to the FE results (solid lines represent the FE results with picture-frame boundary conditions, and the dash line represent the FE results with periodic boundary conditions); the symbols represent the experimental results.

Fig. 8: The FE results of energy absorption of each component in the specimen and the loading plates of the fixture from the FE simulation.

Fig. 9: Parametric study of parameters of a chiral RVE including rib thickness *t*, rib length *l*, and rib angle α_o, and the stiffness ratio between the ribs and added hinges. Solid blue circles represent the FE simulation results. (a) Varying *t* while *l* and α_o are kept the same; (b) varying *l* while *t* and α are kept the same; (c) varying α_o while *t* and *l* are kept the same; (d) varying the stiffness of the added hinges while α_o, *t* and *l* are kept the same.

Fig. 10: (a) R_K vs. E_r/E_h ($l = 5mm, t = 0.2mm, \alpha_o = 90^{\circ}$); (b) The ratio between the effective shear modulus and effective stiffness vs. corner angle (solid lines represent the analytical prediction; symbols represent the FE results, and different colors represent different values of E_r/E_h).

Table Captions:

Table 1: Shear modulus from the experiments and FE simulations ($\gamma < 0.1^{\circ}[1.8(10^{-3})\ rad.]$)

(a)

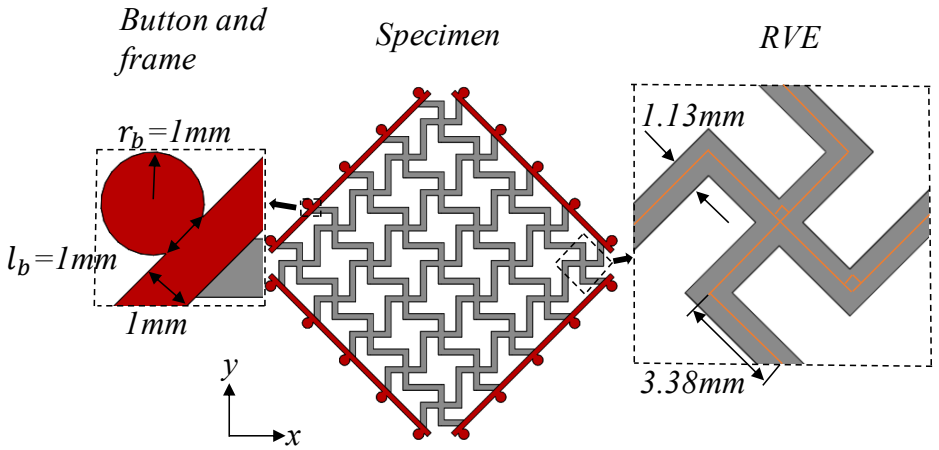
Button and frame
Specimen
RVE
r_b=1mm
l_b=1mm
1mm
1.13mm
3.38mm
y
x

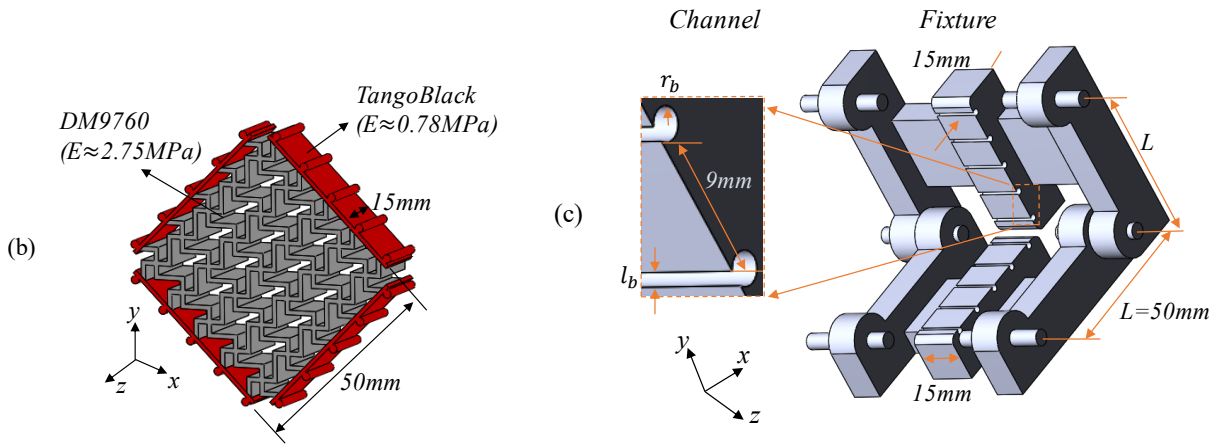

Fig. 1: Dimensions of the (a) specimen in a 2D view, (b) in a 3D view and (c) channels of the fixtures: $L = 50mm$.

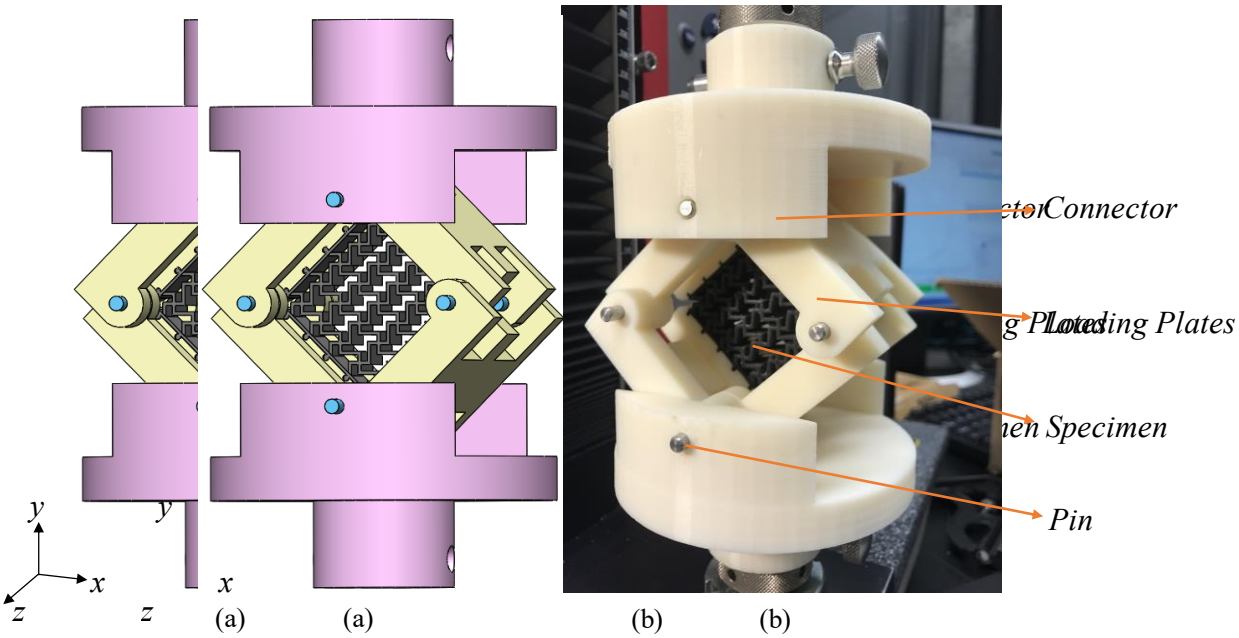

Fig. 2: The picture-frame apparatus: (a) solid model; (b) the 3D printed assembly.

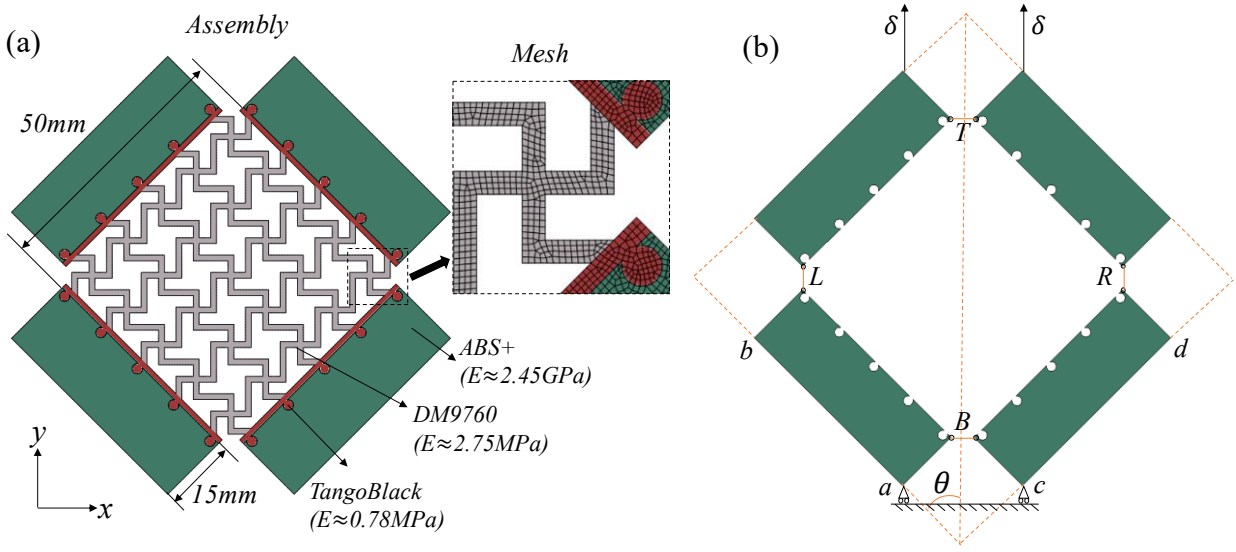

Fig. 3: The FE model: (a) assembly and the mesh, and (b) boundary conditions and the prescribed displacement.

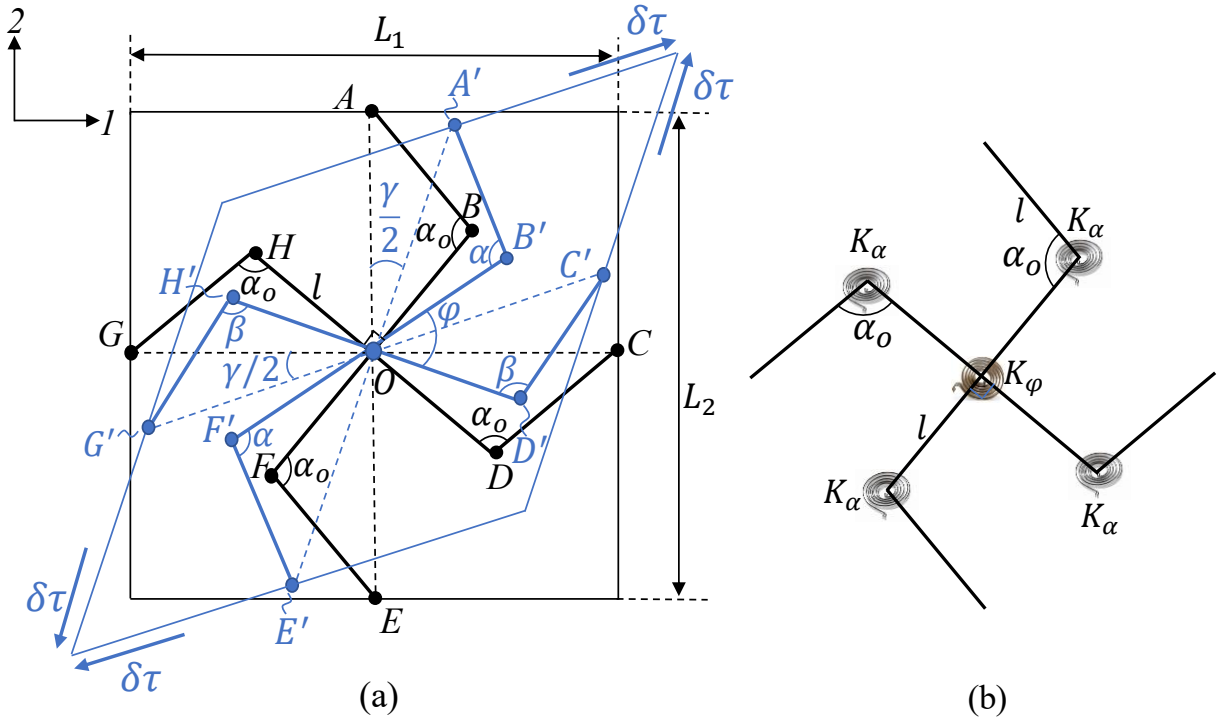

Fig. 4: The schematic drawing of the model RVE under pure shear: (a) the undeformed configuration (black lines) and the deformed configuration (blue lines); (b) the rigid-rod-rotational spring model of an RVE.

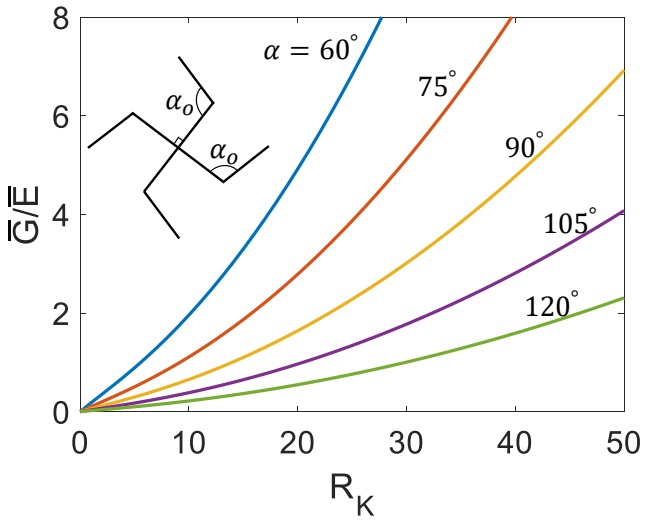

Fig. 5: The ratio between the effective shear modulus and the effective stiffness vs. R_K for various corner angle α_o, predicted by Eq. (10).

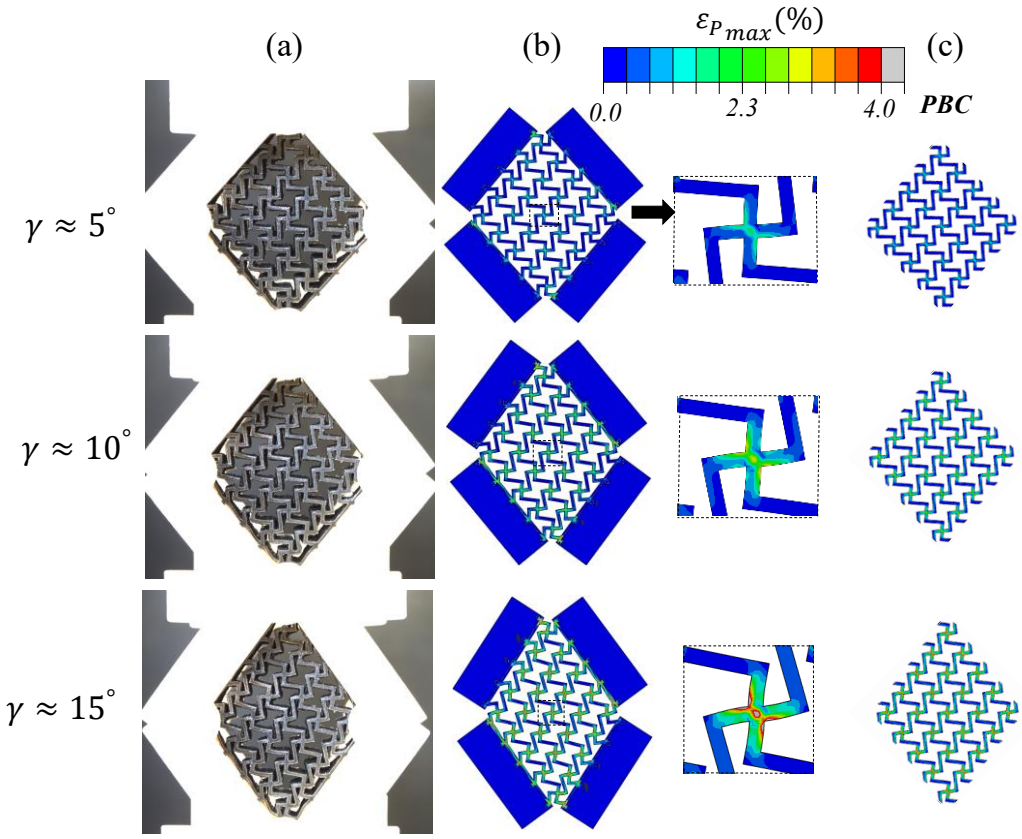

Fig. 6: (a) Snapshots of the deformed specimen from the experiments at the overall shear strain of $\gamma \approx 5^{\circ}$, 10°, and 15°; and the corresponding FE contours of the maximum principal strain with the boundary conditions the same as the experiment (b), and those with periodic boundary conditions (c).

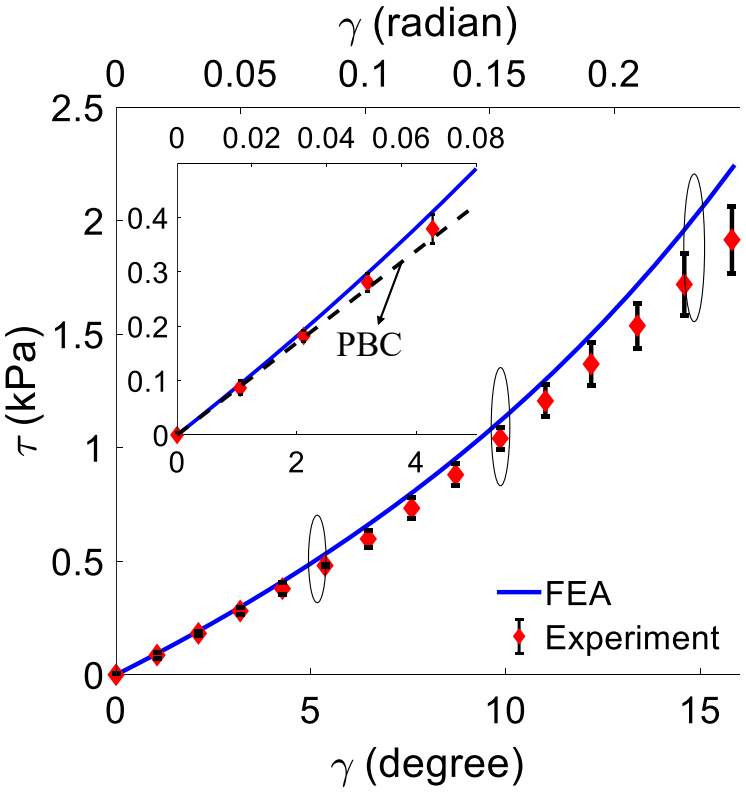

Fig. 7: Shear stress-shear strain curves. The lines refer to the FE results (solid lines represent the FE results with picture-frame boundary conditions, and the dash line represent the FE results with periodic boundary conditions); the symbols represent the experimental results.

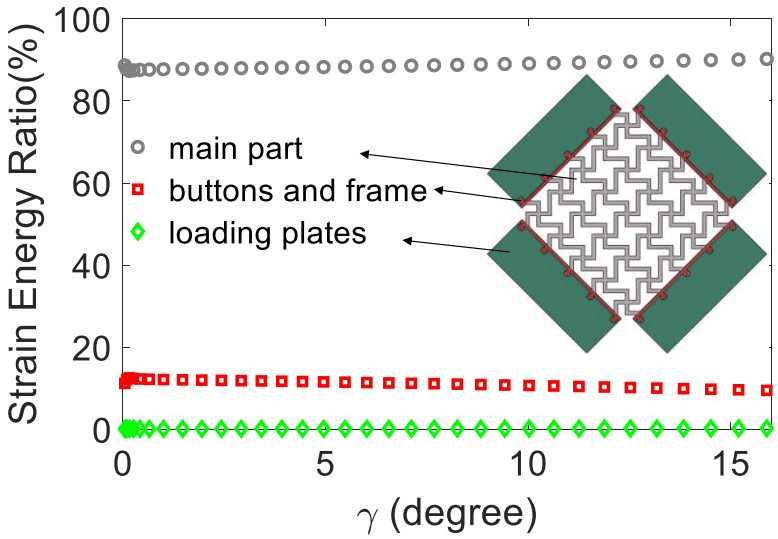

Fig. 8: The FE results of energy absorption of each component in the specimen and the loading plates of the fixture from the FE simulation.

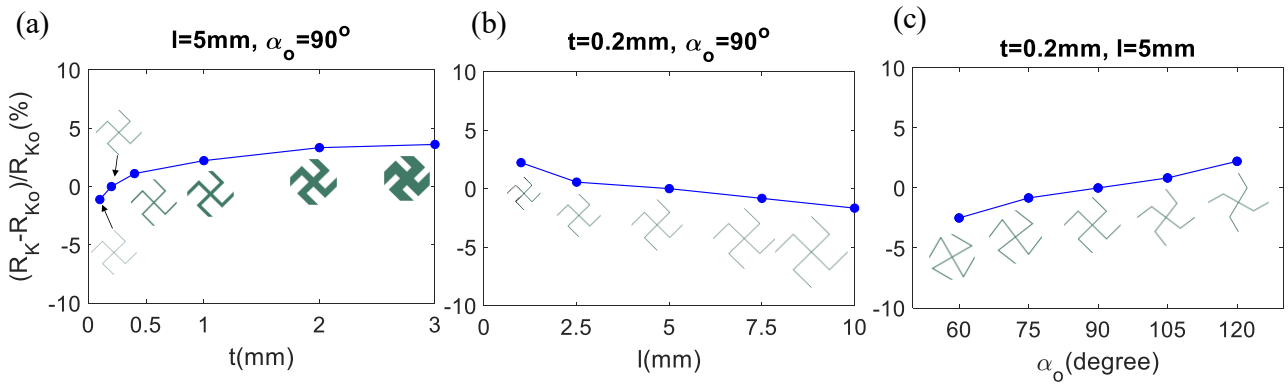

Fig. 9: Parametric study of parameters of a chiral RVE including rib thickness *t*, rib length *l*, and rib angle α_o, and the stiffness ratio between the ribs and added hinges. Solid blue circles represent the FE simulation results. (a) Varying *t* while *l* and α_o are kept the same; (b) varying *l* while *t* and α are kept the same; (c) varying α_o while *t* and *l* are kept the same; (d) varying the stiffness of the added hinges while α_o, *t* and *l* are kept the same.

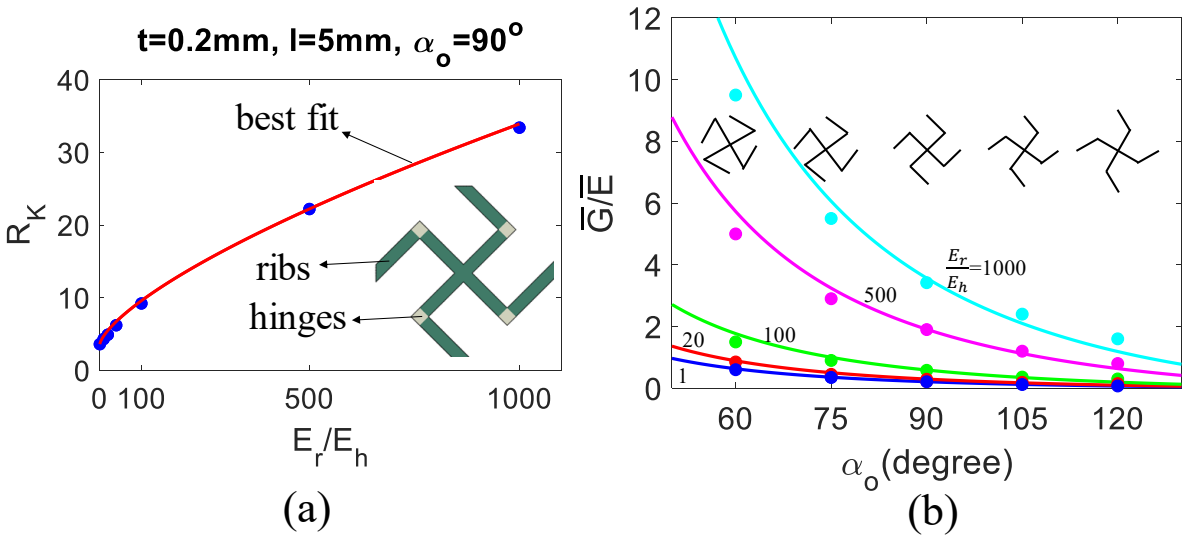

Fig. 10: (a) R_K vs. E_r/E_h ($l = 5mm, t = 0.2mm, \alpha_o = 90^\circ$); (b) The ratio between the effective shear modulus and effective stiffness vs. corner angle (solid lines represent the analytical prediction; symbols represent the FE results, and different colors represent different values of E_r/E_h).

Table 1: Shear modulus from the experiments and FE simulations ($\gamma < 0.1^{\circ}[1.8(10^{-3})\ rad.]$)

	Experiment	FE simulation (PBC)	FE simulation (Picture frame)	Theoretical Prediction
Shear Modulus (kPa)	4.71	4.85	5.10	4.25
Percent difference (%)	/	3.0	8.3	9.8